

# REPORT

Project Title: Implicit and Multigrid Method for Ideal Multigrid  
Convergence

Principal Investigator: Dr. Chaoqun Liu

Institution: Center for Numerical Simulation and Modeling  
College of Engineering and Science  
Louisiana Tech University  
P.O.Box 10348  
Ruston, LA 71272

Grant No.: NAG-1-2136

Dates Covered: 1/99 – 6/99

TO: Barbara Thompson  
Contracting Office  
NASA Langley Research Center  
Hampton, VA 23665

# Direct Numerical Simulation of Separated Flow around NACA 0012 Airfoil (for NAG-1-2136, Project Title: Implicit and Multigrid Method for Ideal Multigrid Convergence)

C. Liu, H. Shan, L. Jiang  
*Center for Numerical Simulation and Modeling  
Louisiana Tech University  
Ruston, Louisiana, U.S.A.*

## Abstract

Numerical investigation of flow separation over a NACA 0012 airfoil at large angles of attack has been carried out. The numerical calculation is performed by solving the full Navier-Stokes equations in generalized curvilinear coordinates. The second-order LU-SGS implicit scheme is applied for time integration. This scheme requires no tridiagonal inversion and is capable of being completely vectorized, provided the corresponding Jacobian matrices are properly selected. A fourth-order centered compact scheme is used for spatial derivatives. In order to reduce numerical oscillation, a sixth-order implicit filter is employed. Non-reflecting boundary conditions are imposed at the far-field and outlet boundaries to avoid possible non-physical wave reflection. Complex flow separation and vortex shedding phenomenon have been observed and discussed.

## 1 Introduction

It is of particular interest to study the flow separations around airfoils at large angle of attack. Flow separations have at least two effects. The first one is the sudden loss of lift, and the second one is the generation of aerodynamic noise. These two aspects are crucial to design of airfoils, and these problems can not be solved in the absence of the detailed information about flow separation, which is a complex time-dependent physical process. Understanding of the process is still a open question for research.

The spatial and temporal complexity of this problem makes it inaccessible by conventional experimental and numerical techniques. From the experimental point of view, as it has been pointed out by Shih, *et al.* (1992), that the level of understanding needs to advance from qualitative conjectures based on flow visualization and/or measurement of global quantities, such as lift and drag, to the quantitative measurement of the instantaneous flow field. The prominent feature about the flow past an airfoil at large angles of attack is the emergence of large-scale vortices when the flow separates from the airfoil surface. The spatial and temporal evolution of these vortical structures dominates the unsteady flow behavior over the airfoil. Detailed information, such as spatial vorticity distribution at each instant, is required to study in this problem. This requirement excludes the use of traditional sing-point velocity measurement techniques, such as hot-wire anemometry or laser Doppler anemometry. A new experimental technique, particle image displacement velocimetry

(PIDV), has been used by Shih, *et al.* (1992) to study the unsteady flow past a NACA 0012 airfoil in pitching-up motion in a water towing tank. The Reynolds number based on the airfoil chord and the freestream velocity is 5000. Instantaneous velocity fields at different time have been acquired over the entire flow field. Using the whole field data, the out-of-plane component of vorticity is computed. They found out that boundary-layer separation near the airfoil leading edge leads to the formation of a vortical structure. This vortex further triggers the shedding of a count-rotating vortex near the trailing edge. The unsteady separated flow near the leading edge and trailing edge of a NACA 0012 airfoil was measured in more details by Shih, *et al.* (1995) using particle image velocimetry (PIV) technique. In his experiment, the Reynolds number was 5000 and 25000, based on the chord of the airfoil and the freestream velocity. The role of the trailing edge flow was also examined. At the late stage, as the primary vortex approach the trailing edge, a counter-rotating vortex is shed from the trailing edge. The experimental results obtained by Shih, *et al.* (1992, 1995) will be compared with our DNS results in Section 3. It is believed by the authors that the generic characteristics of an unsteady separated flow are fairly universal and independent of the Reynolds number and external flow conditions. The Reynolds number has effect on the time and length scales of the separation structure. For example, the separation structure of a low Reynolds number flow evolves faster than a high Reynolds number case. The stronger viscous diffusion of a low Reynolds number flow will thicken the boundary layer and thereby attenuate the explosive nature of the unsteady separation (Shih, *et al.* 1995).

For numerical approaches, Tenaud & Phuoc (1997) used large eddy simulation (LES) to study separated flow around a NACA 0012 airfoil at  $20^\circ$  angle of attack. Three different flow regions following different structure behaviors were observed in their results. The three regions are the leading edge, the middle part of the upper surface, and the trailing.

Both the experimental and numerical studies have achieved significant progress in the past decades. However, the available information is still inadequate to understand the mechanism behind separation thoroughly. Although spatial resolution of a PIV or PIDV is high, the temporal resolution is low because of the limitation of the hardware speed. On the other hand, the LES can achieve a high temporal resolution, but the spatial resolution is not enough to catch all small-scale structures. Direct numerical simulation (DNS) with high order numerical scheme becomes practical as the advances in modern computer power.

This work focuses on direct numerical simulation of flow separation around a NACA 0012 airfoil at large angle of attack, where large vortices are intermittently formed and shed from the leading edge. The separation leads to an alternation of the pressure distribution and therefore changes the lift and moment acting on an airfoil. The aerodynamic forces become unsteady and there is a dramatic decrease in lift accompanied by an increase in drag and large changes in the moment exerted on the airfoil. The interactions between vortices and between vortices and airfoil surface will generate noise. Understanding of flow separation will provide assistance to improving the separation control and noise control. One of the main objectives of the present work is to reveal the detailed separation structures and provide spectrums of the separation signals.

## 2 Governing Equations and Numerical Methods

The two-dimensional Navier-Stokes equations in generalized curvilinear coordinates  $(\xi, \eta)$  are written in conservative forms:

$$\frac{1}{J} \frac{\partial Q}{\partial t} + \frac{\partial(E - E_v)}{\partial \xi} + \frac{\partial(F - F_v)}{\partial \eta} = 0 \quad (1)$$

The flux vectors for flow are

$$\begin{aligned} Q &= \begin{pmatrix} \rho \\ \rho u \\ \rho v \\ e \end{pmatrix} \quad E = \frac{1}{J} \begin{pmatrix} \rho U \\ \rho U u + p \xi_x \\ \rho U v + p \xi_y \\ U(e + p) \end{pmatrix} \quad F = \frac{1}{J} \begin{pmatrix} \rho V \\ \rho V u + p \eta_x \\ \rho V v + p \eta_y \\ V(e + p) \end{pmatrix} \\ E_v &= \frac{1}{J} \begin{pmatrix} 0 \\ \tau_{xx}\xi_x + \tau_{yx}\xi_y \\ \tau_{xy}\xi_x + \tau_{yy}\xi_y \\ q_x\xi_x + q_y\xi_y \end{pmatrix} \quad F_v = \frac{1}{J} \begin{pmatrix} 0 \\ \tau_{xx}\eta_x + \tau_{yx}\eta_y \\ \tau_{xy}\eta_x + \tau_{yy}\eta_y \\ q_x\eta_x + q_y\eta_y \end{pmatrix} \end{aligned}$$

where  $J$  is Jacobian of the coordinate transformation, and  $\xi_x, \xi_y, \eta_x, \eta_y$  are coordinate transformation metrics.

In Eq. (1), the second order Euler Backward scheme is used for time discretization, and the fully implicit form of the discretized equation is:

$$\frac{3Q^{n+1} - 4Q^n + Q^{n-1}}{2J\Delta t} + \frac{\partial(E^{n+1} - E_v^{n+1})}{\partial \xi} + \frac{\partial(F^{n+1} - F_v^{n+1})}{\partial \eta} = 0 \quad (2)$$

$Q^{n+1}$  is estimated iteratively as:

$$Q^{n+1} = Q^p + \delta Q^p \quad (3)$$

$$\delta Q^p = Q^{p+1} - Q^p \quad (4)$$

At step  $p = 0$ ,  $Q^p = Q^n$ ; as  $\delta Q^p$  is driven to zero,  $Q^p$  approaches  $Q^{n+1}$ . Flux vectors are linearized as following:

$$\begin{aligned} E^{n+1} &\approx E^p + A^p \delta Q^p \\ F^{n+1} &\approx F^p + B^p \delta Q^p \end{aligned} \quad (5)$$

So that Eq. (2) can be written as:

$$\left[ \frac{3}{2}I + \Delta t J (D_\xi A + D_\eta B) \right] \delta Q^p = R \quad (6)$$

where  $R$  is the residual:

$$R = -\left( \frac{3}{2}Q^p - 2Q^n + \frac{1}{2}Q^{n-1} \right) - \Delta t J [(D_\xi(E - E_v) + D_\eta(F - F_v))]^p \quad (7)$$

The superscript  $p$  stands for iteration step.  $D_\xi, D_\eta$  represent partial differential operators,  $A, B$  are the Jacobian matrices of flux vectors:

$$A = \frac{\partial E}{\partial Q}, \quad B = \frac{\partial F}{\partial Q} \quad (8)$$

The right hand side of Eq. (6) is discretized using the fourth-order compact scheme (Lele, 1992) for spatial derivatives, and the left hand side of the equation is discretized following LU-SGS method (Yoon & Kwak, 1992). In this method, the Jacobian matrices of flux vectors are split as:

$$A = A^+ + A^-, \quad B = B^+ + B^- \quad (9)$$

where,

$$\begin{aligned} A^\pm &= \frac{1}{2}[A \pm r_A I] \\ B^\pm &= \frac{1}{2}[B \pm r_B I] \end{aligned} \quad (10)$$

where,

$$\begin{aligned} r_A &= \kappa \max[|\lambda(A)|] + \tilde{\nu} \\ r_B &= \kappa \max[|\lambda(B)|] + \tilde{\nu} \end{aligned} \quad (11)$$

where  $\lambda(A), \lambda(B)$  are eigenvalues of  $A, B$  respectively,  $\kappa$  is a constant greater than 1.  $\tilde{\nu}$  represents the effects of viscous terms. The following expression is used.

$$\tilde{\nu} = \max\left[\frac{\mu}{(\gamma - 1)M_r^2 R_e P_r}, \frac{4}{3} \frac{\mu}{R_e}\right] \quad (12)$$

The first-order upwind finite difference scheme is used for the split flux terms on the left hand side of Eq. (6). This does not effect the accuracy of the final solution. As the left hand side is driven to zero, the discretization error of the left hand side will also be driven to zero. The finite difference representation of Eq. (6) can be written as:

$$\begin{aligned} \left[\frac{3}{2}I + \Delta t J(r_A + r_B)I\right] \delta Q_{i,j}^p &= R_{i,j}^p \\ -\Delta t J \quad &\begin{bmatrix} A^- \delta Q_{i+1,j}^p - A^+ \delta Q_{i-1,j}^p \\ + B^- \delta Q_{i,j+1}^p - B^+ \delta Q_{i,j-1}^p \end{bmatrix} \end{aligned} \quad (13)$$

In LU-SGS scheme, Eq. (13) is solved by three steps. First we initialize  $\delta Q^0$  using

$$\delta Q_{i,j}^0 = \left[\frac{3}{2}I + \Delta t J(r_A + r_B)I\right]^{-1} R_{i,j}^p \quad (14)$$

In the second step, the following formula is used:

$$\begin{aligned} \delta Q_{i,j}^* &= \delta Q_{i,j}^0 \\ &+ \left[\frac{3}{2}I + \Delta t J(r_A + r_B)I\right]^{-1} \\ &\times [\Delta t J(A^+ \delta Q_{i-1,j}^* + B^+ \delta Q_{i,j-1}^*)] \end{aligned} \quad (15)$$

For the last step,  $\delta Q^p$  is obtained by

$$\begin{aligned}\delta Q_{i,j}^p &= \delta Q_{i,j}^* \\ &- \left[ \frac{3}{2}I + \Delta t J(r_A + r_B) \right]^{-1} \\ &\times [\Delta t J(A^- \delta Q_{i+1,j}^p + B^- \delta Q_{i,j+1}^p)]\end{aligned}\quad (16)$$

The sweeping is performed along the planes of  $i + j = \text{const}$ , i.e in the second step, sweeping is from the low-left corner of the grid to the high-right corner, and then vice versa in the third step.

In order to depress numerical oscillation caused by central difference scheme, spatial filtering is used instead of artificial dissipation. The implicit sixth-order compact scheme for space filtering (Lele, 1992) is applied for primitive variables  $u, v, \rho, p$  after each time step.

For subsonic flow,  $u, v, T$  are prescribed at the upstream boundary,  $\rho$  is obtained by solving the modified N-S equation based on characteristic analysis. On the far field and out flow boundary, non-reflecting boundary conditions are applied. Adiabatic, non-slipping condition is used for the wall boundary. All equations of boundary conditions are solved implicitly with internal points. Specific details of boundary treatment can be found in Jiang *et al*, (1999)

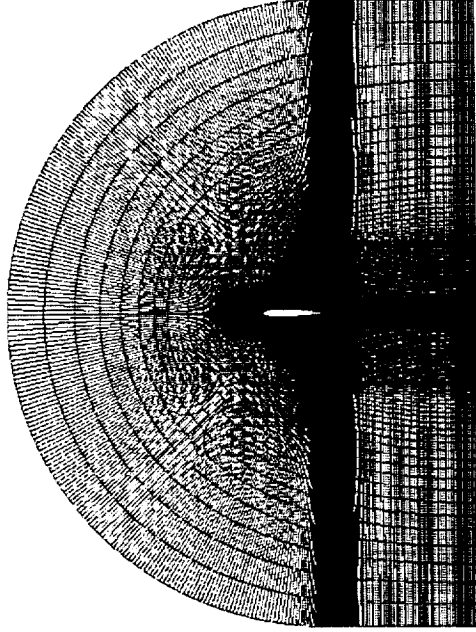
### 3 Numerical Grid Generation

An elliptic grid generation method first proposed by Spekreijse (1995) is used to generate 2D grids. The elliptic grid generation method is based on a composite mapping, which consists of a nonlinear transfinite algebraic transformation and an elliptic transformation. The algebraic transformation maps the computational space onto a parameter space, and the elliptic transformation maps the parameter space on to the physical domain. The elliptic transformation is carried by solving a set of Poisson equations. The control functions are specified by the algebraic transformation only and it is, therefore, not needed to compute the control functions at the boundary and to interpolate them into the interior of the domain, as required by the well-known elliptic grid generation systems based on Poisson systems (Thompson *et al*, 1985). The orthogonality of grids on the body surface or near the boundary is attainable by re-configuration of the algebraic transformation. The grid number is  $841 \times 141$  along the streamwise direction and the wall normal direction, respectively.

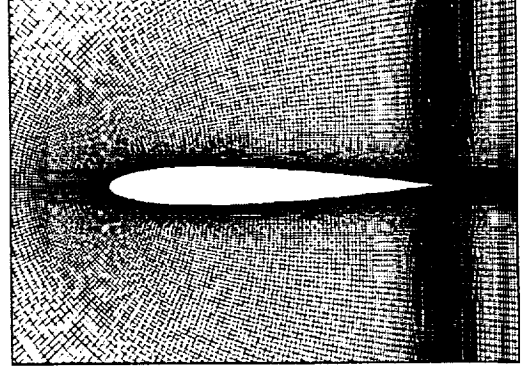
In Figure 1, the body-fitted C-grid around a NACA 0012 airfoil is displayed. The grids are orthogonal at the boundaries. The distribution of the grids near the leading-edge and trailing-edge are also depicted by Figure 1(c) and (d), where good orthogonality has been achieved.

### 4 Results and Discussions

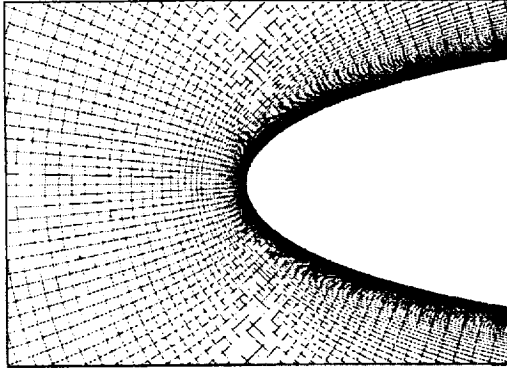
The situation of an airfoil with a high angle of attack occurs in many applications which are of particular interest. In these cases, the fluid flow around the airfoil becomes very unstable and different eddy structures are formed in the vicinity of the airfoil. These eddy structures severely affect the airfoil's aerodynamic properties. Vortex interactions, such as vortex pairing, and the interactions between the airfoil and vortex, lead to noise generation. In our simulation, two angles of attack have been chosen, the first one is  $\alpha = 12^\circ$ , the second one is  $\alpha = 20^\circ$ . For both cases, the Reynolds number is  $Re = 5 \times 10^5$ , based on the chord length  $L$  and freestream velocity  $U$ .



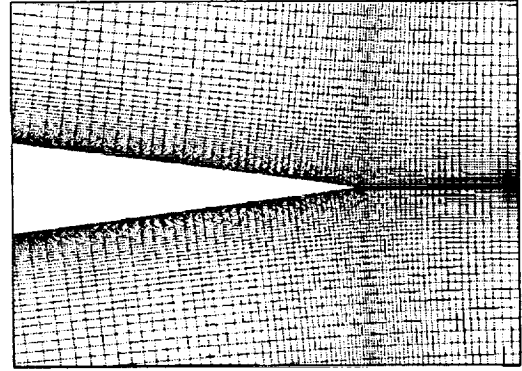
(a) overview of the grids



(b) grid near airfoil surface



(c) grids near the leading-edge



(d) grids near the trailing edge

Figure 1: C-grid around a NACA 0012 airfoil

#### 4.1 Angle of attack $\alpha = 12^\circ$

In the first case, the flow around a NACA 0012 airfoil at 12 degree angle of attack is simulated. The flow separation process is found unsteady as the flow field is recorded every 1000 time steps, where the time step is approximately  $\Delta t = 1.767 \times 10^{-4}$ . An animation of the flow field has been made based on the data recorded. In Figure 2, the contours of the spanwise vorticity at different time are displayed, where the time interval between the adjacent frames is  $0.884L/U$ , and  $L$  is the chord of the airfoil,  $U$  is the freestream velocity. For each frame, the area near the trailing edge are enlarged and displayed in Figure 3. In frame (b) of Figure 2, a separation bubble is observed

near the leading edge. The leading-edge separation bubble is formed when the laminar boundary layer separates from the surface as a result of the strong adverse pressure gradient downstream of the point of minimum pressure. The separation bubble is unstable. Vortical structures shed from the separation and move downstream along the airfoil surface. These vortical structures are called the primary vortices. The primary vortices shed from the leading are rolling clockwise and moving downstream at the same time. Strong shear layers with reversed vorticity are generated near the wall below the primary vortices as a result of the induced motion of these vortices. For example, in the vicinity of leading edge in frames (e) (i) (p) (q) of Figure 2, this phenomenon is quite clear. The primary vortices are pushed away from the wall by the induced reversed vorticity. Some primary vortices reattach on the airfoil surface where they encounter a slower convection velocity and slow down in motion to downstream. These reattached primary vortices are caught by upstream vortices which are moving faster downstream, and vortex merge happens when the vortex undergoing reattachment is overtaken by an upstream vortex with the same rotating direction and the two vortices eventually merge in one large vortex rotating in the original direction; (see frames (e) (f) (h) (o) (p)). The reattachment of the primary vortex leads to strong interaction between the vortex and the local boundary-layer and induces an upstream accumulation and eruption of a reversed boundary-layer vorticity. The reversed vorticity interacts with the primary vortex to form a counter-rotating vortex pair. The reversed vortex induces the primary vortex upward away from the wall. The vortex pair move downstream more rapidly with a faster convection velocity. The vortex pair can be seen in frames (g) (j) (n) (o) of Figure 2. The reattachment of the primary vortex happens not only near the leading edge but also at the rear part of the suction surface. In frame (g) of Figure 2, two vortex pairs are observed. The upstream one is formed by a primary reattachment near the leading edge, while the downstream one is formed by a primary vortex reattachment at the rear part of the airfoil. For each vortex pair, the interactions between these vortices lead to vortex deformation shown in frame (h) of Figure 2, where the vortex system becomes very complex because of the interaction and deformation. Similar phenomena of vortex pairing have been observed in experiments, e.g. Shih, *et al.* (1992). Another interesting phenomenon is observed near the trailing edge of the airfoil in frame (i) and (j) of Figure 2, where a strong counterclockwise rotating vortex is generated by the sweeping of the clockwise rotating vortex system over the trailing edge. When the clockwise rotating vortex shed from the leading edge reaches the trailing edge, it induces a local low pressure which drives the lower surface separating layer across the wake and curve into the upper surface. This lower surface shear layer quickly rolls into the intense counterclockwise vortex. This process can be seen more clearly in frame (h) and (i) of Figure 3. This phenomenon was also observed in experiments (Shih, *et al.* 1992, 1995). The experimental results and our DNS results agree well qualitatively. The quantitative comparison is improper because of the difference in Reynolds number. Strong shear layer appears near the downstream edge of this large-scale trailing edge vortex. Because of the instability of the shear layer, a chain of small-scale vortical structures appear along the edge of the large-scale vortex. The structure of these small-scale vortices are similar to that of the Kelvin-Helmholtz type instability. The large-scale vortex moves away from the trailing edge as a result of the self-induced motion, and eventually detaches from the trailing edge, as it is displayed in frames (i) to (k) of Figure 3. A similar process of the generation and detachment of the trailing edge vortex can also be found through frames (u) to (x) in Figure 3. The continuous generation of the trailing edge vortex is quasi-periodic. The interactions between the vortex system are very complex and severe deformations are observed in frames (h) (i) (p) (q) (s) (t) (v) (x) of Figure 2. Near trailing edge, some of the typical vortex deformation are displayed in frames (h) (i) (p) (q) of Figure 3.

To obtain the spectrum information about flow separation, twelve points are selected near the



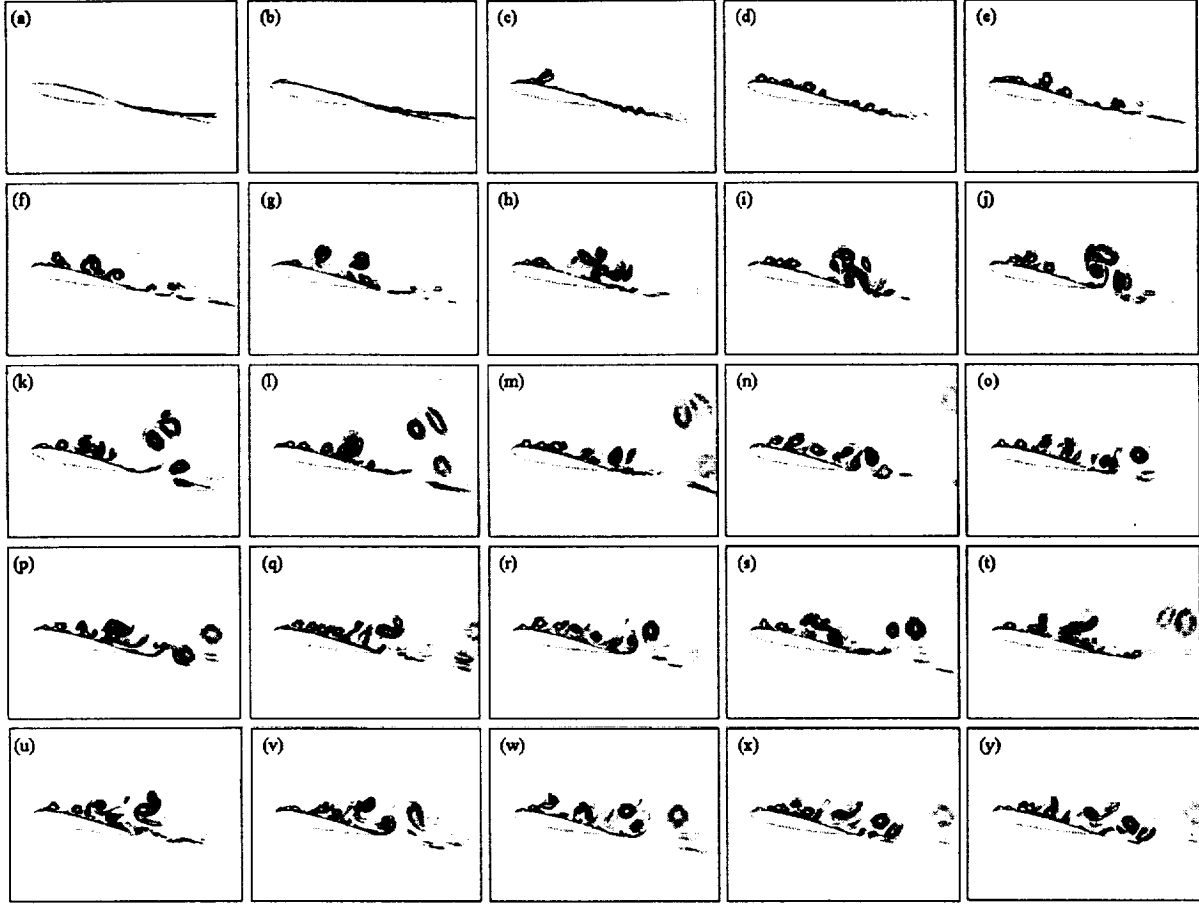


Figure 2: Contours of spanwise vorticity at different time.  $Re = 5 \times 10^5$ ,  $\alpha = 12^\circ$

airfoil surface and in the wake to record the time series of instantaneous velocity and pressure. The location of these points are denoted by P1 – P12 and shown in Figure 4. Points P1 – P10 locate above and very close to the suction surface of the airfoil. Points P11, P12 are in the wake.

The instantaneous fluctuations of the streamwise velocity and pressure at location point P1 and their power spectrum are displayed in Figure 5 – Figure 8. Here, the mean flow are defined based on the temporal average. Figure 6 shows the power spectrum of streamwise velocity fluctuations, where the first peak associated with the slow variation of mean flow is ignored. The frequency of the second and the third peak is  $f = 1.28$ ,  $f = 1.81$ . In this case, the vortices shed from the leading edge intermittently, as it can be seen in Figure 5, where the high frequency oscillations of  $u'$  are linked to vortex shedding. In the spectrum of Figure 6, the high frequency is  $f = 1.81$ , which reflects the frequency of continuous vortex shedding. The lower  $f = 1.28$  is thought to reflect the intermittent feature of vortex shedding. The spectrum of pressure fluctuations exhibit almost the same peak frequency, e.g.  $f = 1.28$  and  $f = 1.79$ .

Figure 9 – 12 show the time series of streamwise velocity, pressure and their spectrums at point P3. At this point, the signals of streamwise velocity and pressure are similar to those at point P1. The frequencies obtained from the velocity and pressure signals are almost the same. The peak frequency is  $f = 1.70$ , which is close to the vortex shedding frequency at P1.

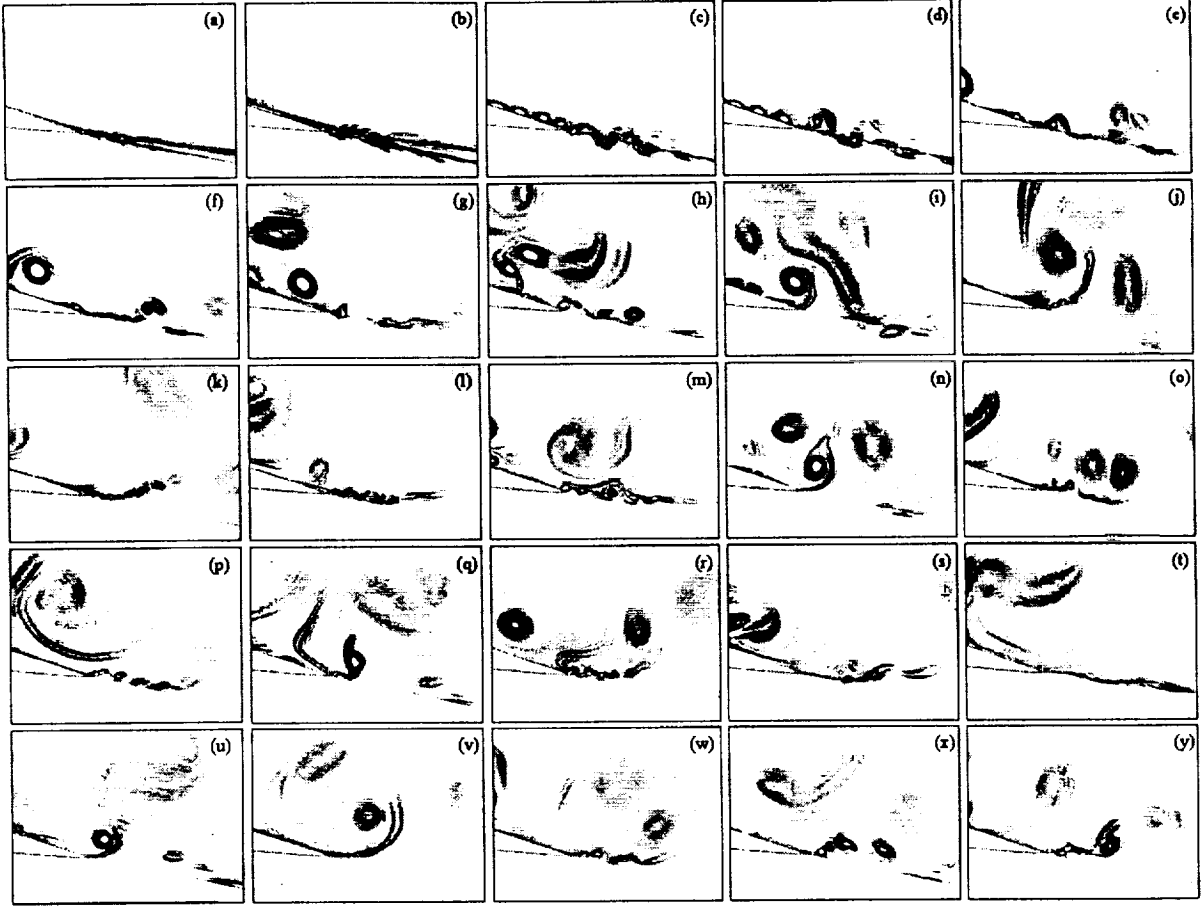


Figure 3: Contours of spanwise vorticity at different time.  $Re = 5 \times 10^5$ ,  $\alpha = 12^\circ$

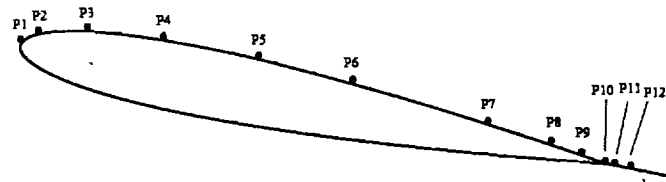


Figure 4: Location points P1 – P12 where the time series are recorded

Figure 13 – 16 show the time series of streamwise velocity and pressure and their spectrums at point P5. The instantaneous velocity and pressure are more regular compared with those at P1. As a matter of fact, the signals recorded at P5 represent the reattachment of the primary vortex, as it is displayed in frames (f) (h) of Figure 2. The primary vortices shed from the leading edge rotate clockwise. When a vortex reattaches near point P5, which is close to the wall, the recorded streamwise velocity decrease, while the vortex also causes the pressure to decrease. Therefore, the streamwise velocity signal is in phase with pressure signal, as it is shown in Figure 13 and Figure 15. In Figure 13 and Figure 15, the low velocity and low pressure points are corresponding to the

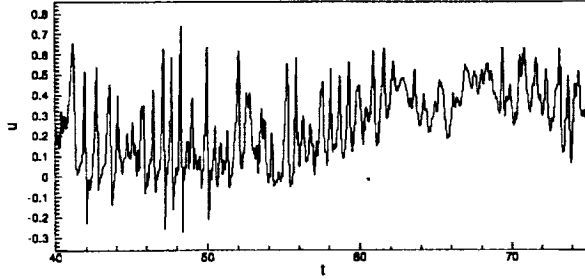


Figure 5: Instantaneous streamwise velocity at location point P1

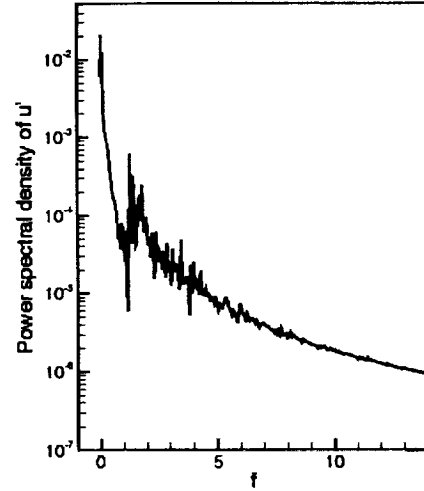


Figure 6: Power spectrum density of  $u'$  at location point P1

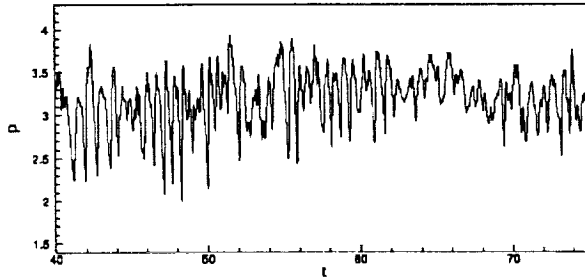


Figure 7: Instantaneous pressure at location point P1

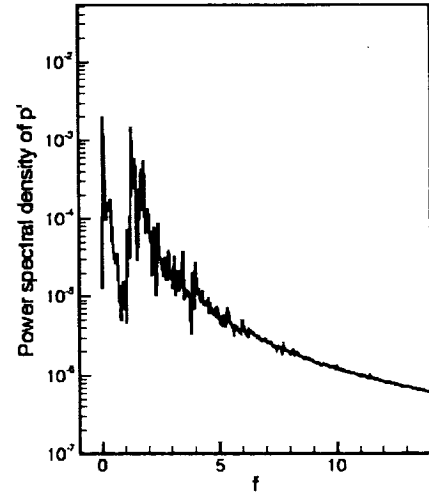


Figure 8: Power spectrum density of  $p'$  at location point P1

vortex reattachment. The frequencies obtained from the velocity and pressure signals are almost the same. The frequency corresponding to the vortex reattachment is  $f = 0.29$ .

Point P9 locates right above the suction surface near the trailing edge. In Figure 3, large scale vortex is found near the trailing edge. The signals recorded at point P9 is used to analyze the frequency feature of the trailing edge vortex. The instantaneous fluctuations of streamwise velocity and pressure at P9 and their power spectrum are displayed in Figure 17 – Figure 20. Both the velocity and pressure signals at point P9 are dominated by low-frequency oscillations. It is also interesting to notice that at this point, the streamwise velocity is opposite in phase to pressure, i.e., the streamwise velocity decreases as pressure increases. A brief explanation is given here based on the fact that the trailing vortex rotates counterclockwise. As the trailing vortex appears, at point P9 close to wall, the induced motion of the vortex increases the streamwise velocity, while

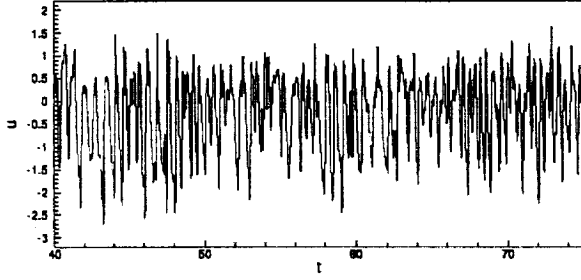


Figure 9: Instantaneous streamwise velocity at location point P3

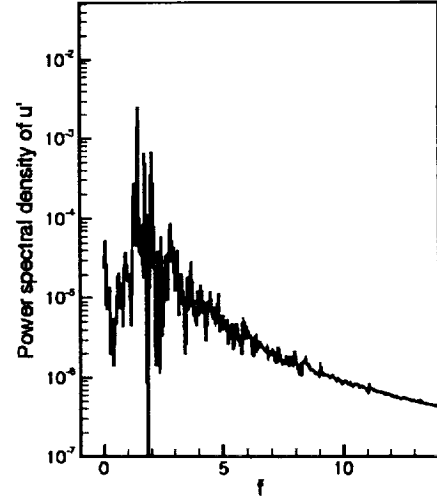


Figure 10: Power spectrum density of  $u'$  at location point P3

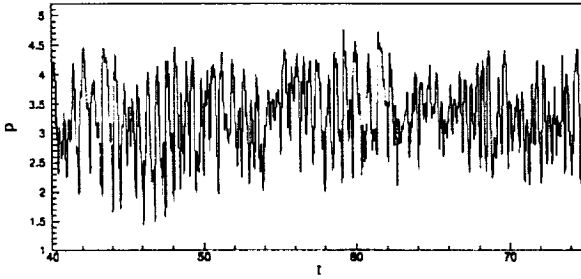


Figure 11: Instantaneous pressure at location point P3

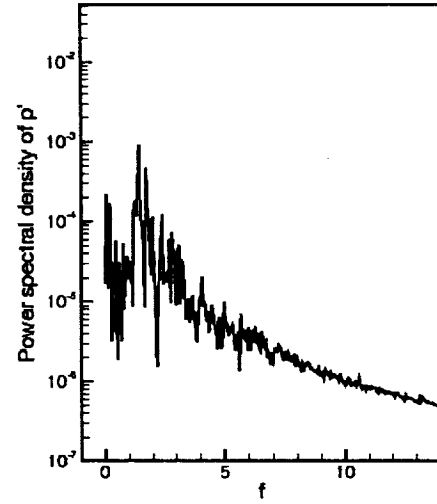


Figure 12: Power spectrum density of  $p'$  at location point P3

the pressure decreases. At this point, the peak frequency for velocity is  $f = 0.24$  and  $f = 0.28$  for pressure.

Now we focus on the next location point P11, which locates in the wake but still close to the trailing edge. High-frequency oscillations appear on streamwise velocity and pressure displayed in Figure 21 and 23, respectively. The high-frequency oscillations associated with the small-scale vortex structures appear from the trailing edge along the edge the large-scale trailing edge vortex, as shown in frames (i), (j) (k) of Figure 3. The high-frequency parts are modulated by the low-frequency signals corresponding to the large-scale trailing edge vortex.

Point P12 locates at downstream of P11, the signals recorded at initial stage at P12 corresponding to frame (a) to (c) in Figure 3 are displayed from Figure 25 to Figure 28. The regular pattern

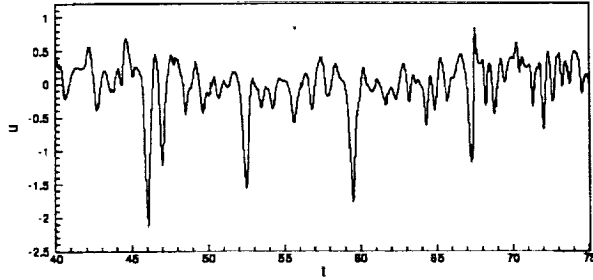


Figure 13: Instantaneous streamwise velocity at location point P5

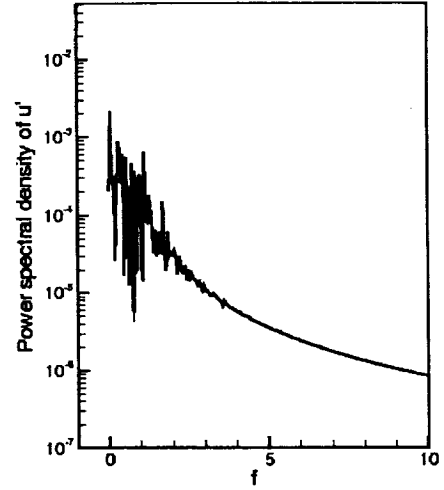


Figure 14: Power spectrum density of  $u'$  at location point P5

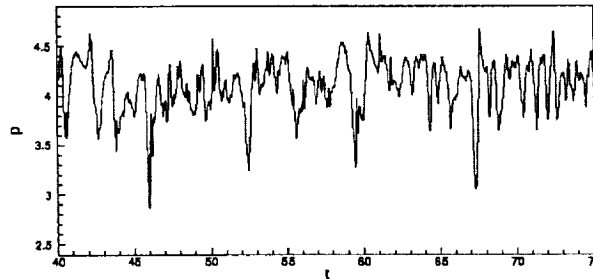


Figure 15: Instantaneous pressure at location point P5

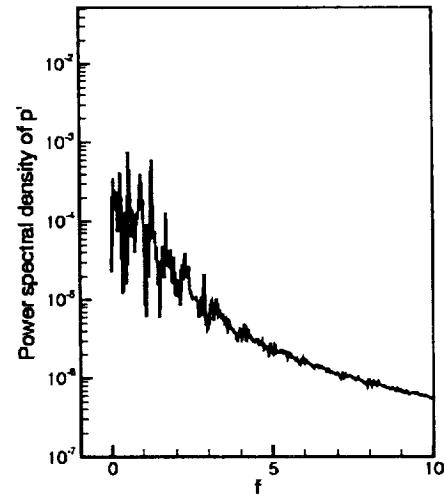


Figure 16: Power spectrum density of  $p'$  at location point P5

of the velocity and pressure indicate the typical Kelvin-Helmholtz type instability.

## 4.2 Angle of attack $\alpha = 20^\circ$

In the second case, the flow around a NACA 0012 airfoil at 20 degree angle of attack is simulated. The Reynolds number  $Re = 5 \times 10^5$ , based on the chord length and freestream velocity. The contours of the spanwise vorticity at various time steps are shown in Figure 29. The flow fields near the trailing edge are displayed by an enlarged view in Figure 30. The time interval between the adjacent frames is  $0.884L/U$ , where  $L$  is chord of the airfoil, and  $U$  is freestream velocity.

In frame (a) of Figure 29, vortices are shedding from the leading edge separation and rotating

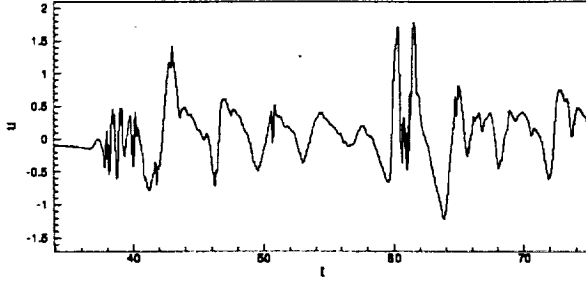


Figure 17: Instantaneous streamwise velocity at location point P9

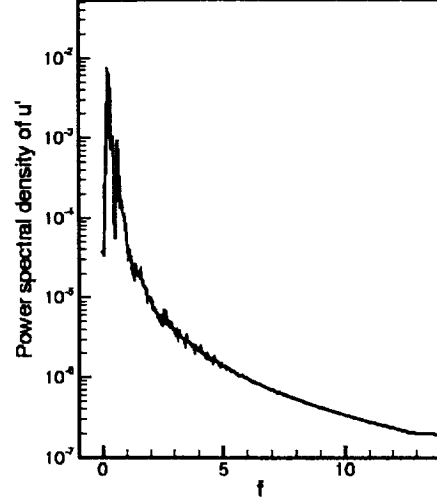


Figure 18: Power spectrum density of  $u'$  at location point P9

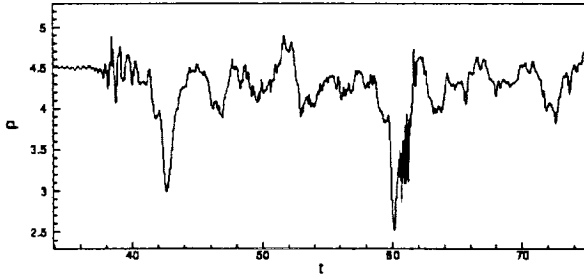


Figure 19: Instantaneous pressure at location point P9

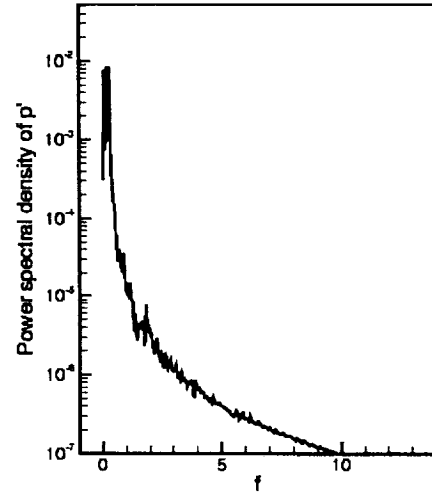


Figure 20: Power spectrum density of  $p'$  at location point P9

clockwise. The clockwise-rotating vortex induces an counterclockwise-rotating vortex near the wall. The interactions between these two vortices forms a counter-rotating vortex pair, which is similar to those observed in the  $\alpha = 12^\circ$  case. The two vortices belonging to the same vortex pair experience strong deformations because of the induced motion (see frame (c) and (d) of Figure 29). A chain of vortices shedding from the leading edge can be seen in frames (e) (j) (p) (q) (r) and (s) of Figure 29, and the position of these vortices are relatively far from the wall compared to those in the  $\alpha = 12^\circ$  case, e.g. frames (d) (i) (q) and (r) in Figure 2. These clockwise-rotating vortices are termed as the primary vortices. The deformation of the vortex pair is more complex compared with the  $\alpha = 12^\circ$  case (see frames (g) (h) (i) and (l) of Figure 2). The observed vortex pair is consistent with the description give by experimental results of Shih, *et al*, (1992, 1995).

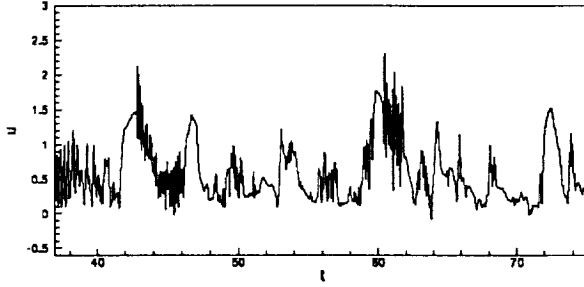


Figure 21: Instantaneous streamwise velocity at location point P11

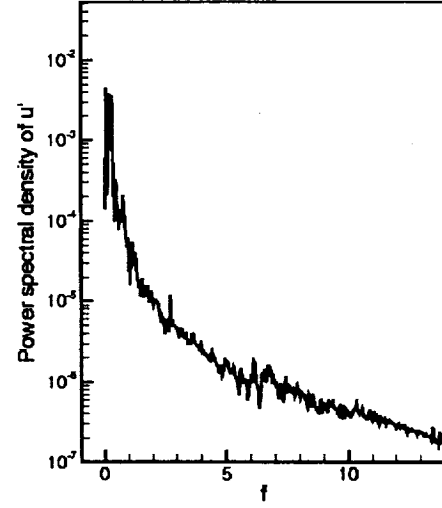


Figure 22: Power spectrum density of  $u'$  at location point P11

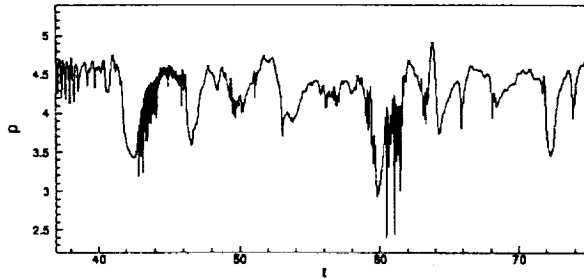


Figure 23: Instantaneous pressure at location point P11

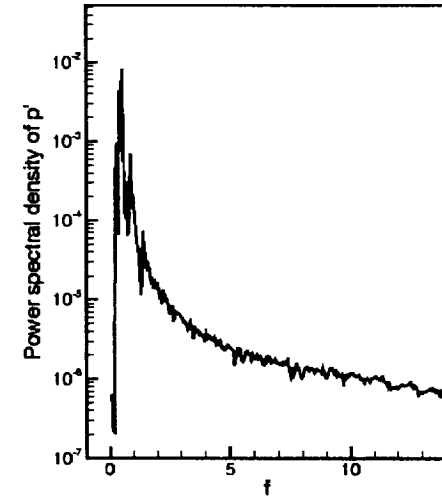


Figure 24: Power spectrum density of  $p'$  at location point P11

In Figure 30, the trailing edge vortices are displayed in more details. Before the primary vortices arrive at the trailing edge, the wake flow exhibits the Kelvin-Helmholtz type instability, see frame (b) and (c) of Figure 30. When the clockwise rotating primary vortex reaches the trailing edge, it induces a local low pressure which drives the lower surface separating layer across the wake and curve into the upper surface. This lower surface shear layer quickly rolls into the intense counterclockwise vortex, e.g. frame (g) of Figure 30. Shortly after the emergence of the trailing vortex, the Kelvin-Helmholtz type small vortices disappear in the wake. As the trailing edge vortex grows, some small-scale vortices appear at the downstream edge of the trailing edge vortex, where the separating trailing edge shear layer locates. These small-scale vortices bear similarity with the Kelvin-Helmholtz type instability (see frame (h) of Figure 30). The large-scale counterclockwise

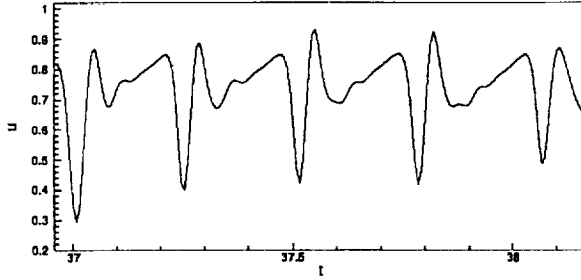


Figure 25: Early stage of the instantaneous stream-wise velocity at location point P12

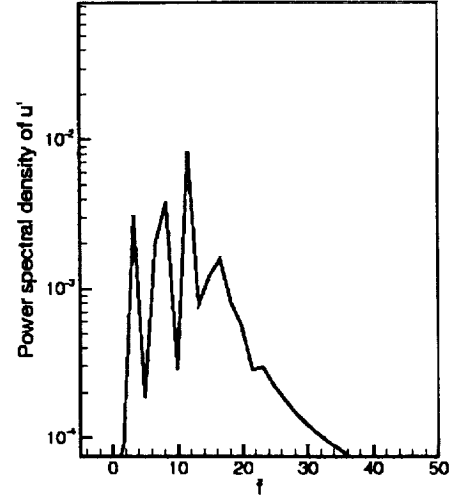


Figure 26: Power spectrum density of signal  $u'$  in Figure 25

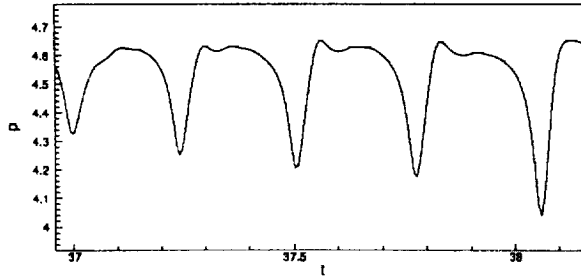


Figure 27: Early stage of the instantaneous pressure at location point P12

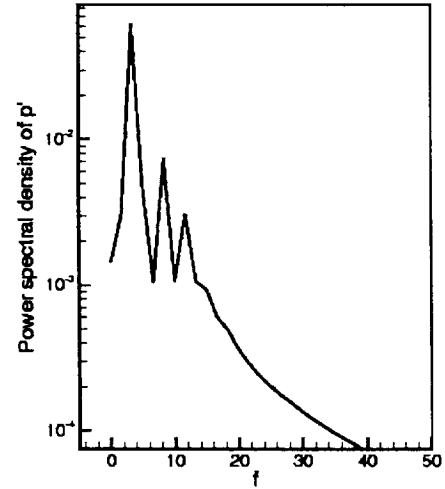


Figure 28: Power spectrum density of signal  $p'$  in Figure 27

rotating vortex moves away from the trailing edge as a result of the self-induced motion, and eventually detaches from the trailing edge (see frame (i) of Figure 30). The detached vortex is brought downstream by convection and it drives the curved shear layer back into the wake. At the same time, the small-scale vortices disappear and the separating shear layer become stable (see frames (j) and (k) of Figure 30). As the trailing edge vortex leaves, the Kelvin-Helmholtz type instability become visible again in the wake (see frame (l) of Figure 30). The evolution of the trailing edge vortex is displayed through frame (g) to frame (l) in Figure 30. A similar process is observed through frame (m) to frame (r) in the same figure. This phenomenon appears quasi-periodically.

Similarly to the  $12^\circ$  case, twelve location points denoted by P1 –P12 are chosen near the airfoil surface and in the wake to record the time series of instantaneous velocity and pressure. The



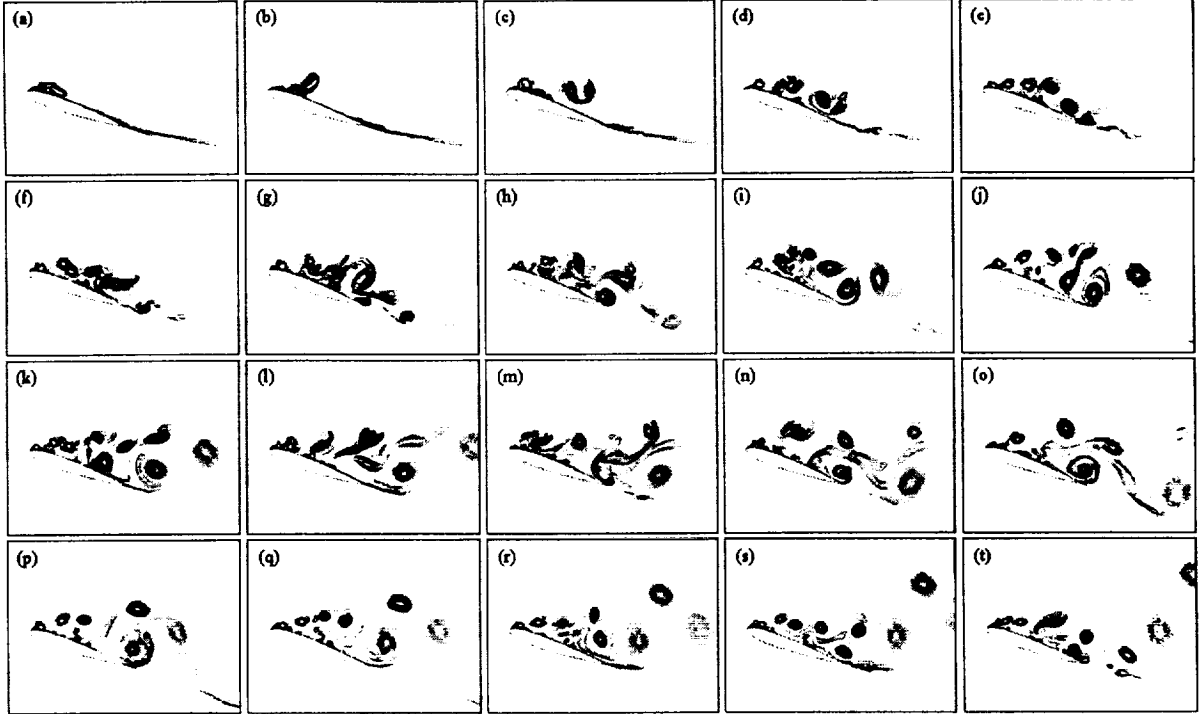


Figure 29: Contours of spanwise vorticity at different time.  $Re = 5 \times 10^5$ ,  $\alpha = 20^\circ$

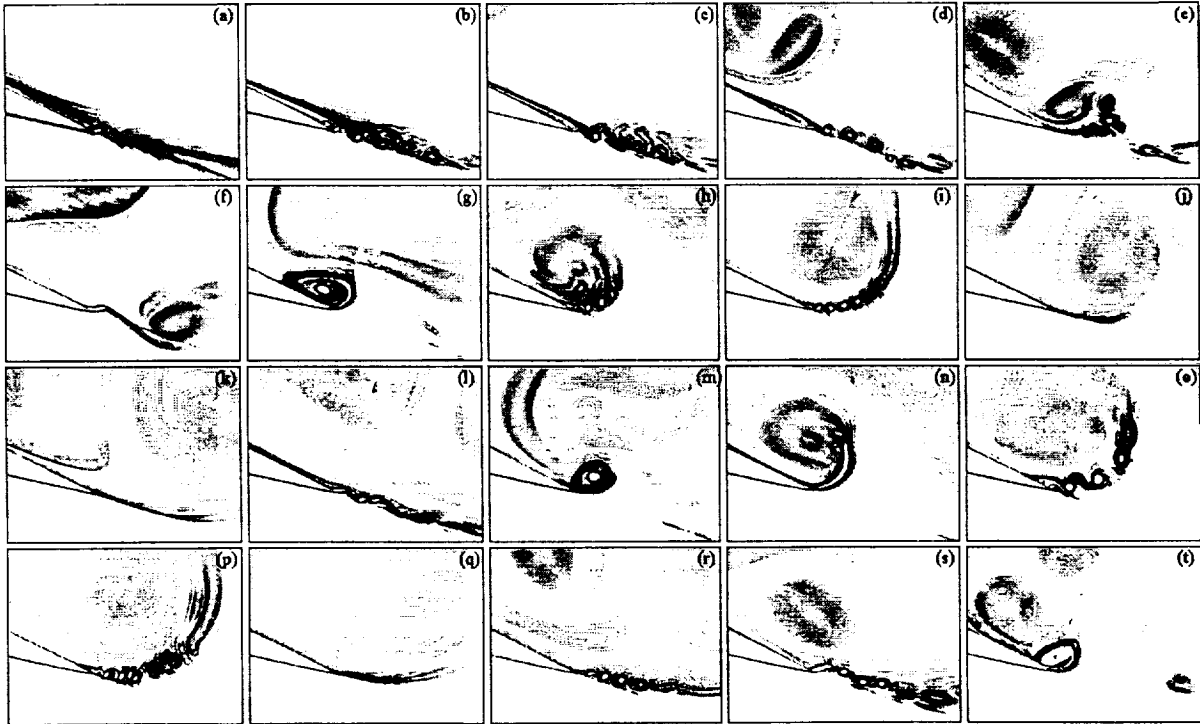


Figure 30: Contours of spanwise vorticity at different time.  $Re = 5 \times 10^5$ ,  $\alpha = 20^\circ$

locations of P1 – P12 are shown in Figure 31. P1 – P10 are near the airfoil surface, and P11, P12 are in the wake.

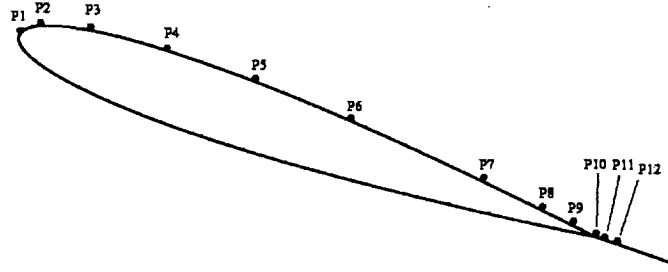


Figure 31: Location points P1 – P12 where the time series are recorded

The instantaneous fluctuations of streamwise velocity and pressure and their power spectrums at point p1 are displayed in Figure 32 – Figure 35. Several peaks can be observed in Figure 33, e.g.  $f = 1.23$ ,  $f = 2.25$ ,  $f = 3.50$ , and  $f = 4.89$ . The dominant  $f = 2.25$  represents the vortex shedding frequency. Thus the Strouhal number is about 2.25. The frequency  $f = 2.25$  also appears in the spectrum for pressure. But the peak frequency of pressure is  $f = 0.27$  which reflects the slow variation of the mean pressure.

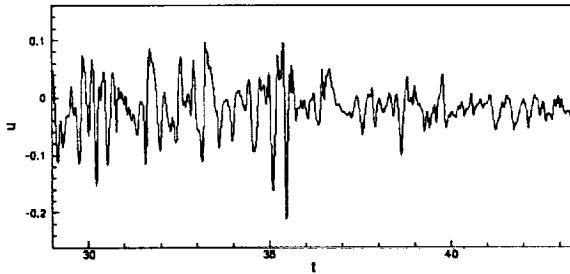


Figure 32: Instantaneous streamwise velocity at location point P1

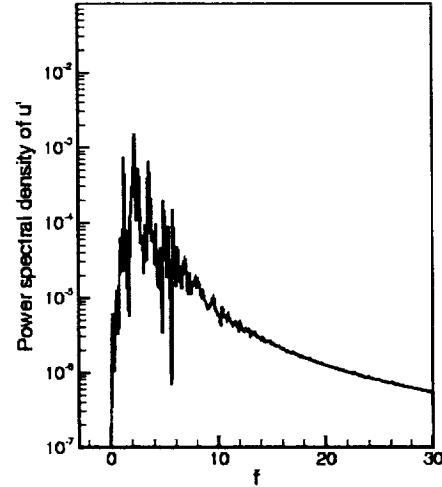


Figure 33: Power spectrum density of  $u'$  at location point P1

At the location of point P3, the reattachment of some primary vortices is observed, e.g. frames (c) (h) (l) (n) (p) and (s) of Figure 29. Figure 36 – 39 display the time series of streamwise velocity, pressure and their spectrums at P3. The instantaneous velocity and pressure are less chaotic compared with those at P1. It is displayed by the spectrums that the dominant frequency is  $f = 1.02$  for streamwise velocity and  $f = 1.15$  for pressure. This frequency is thought to be the frequency of vortex reattachment, which is lower than the frequency of vortex shedding from the leading edge. The vortices shed from the leading edge are clockwise rotating, as a result both streamwise velocity and pressure decrease as the vortices approach the location of point P3 which

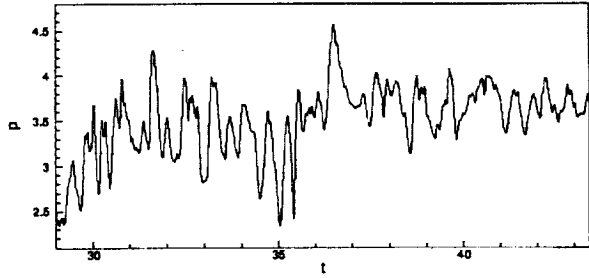


Figure 34: Instantaneous pressure at location point P1

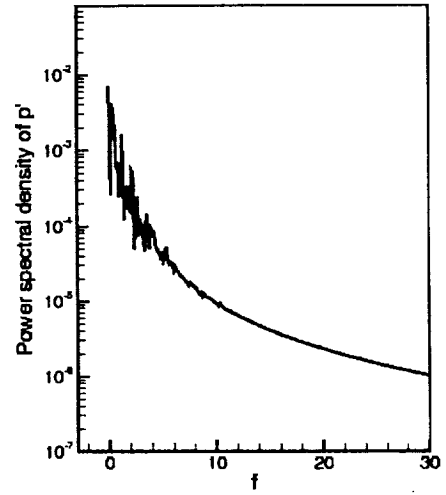


Figure 35: Power spectrum density of  $p'$  at location point P1

is close to the wall. Therefore the streamwise velocity is in the same phase as pressure, as it is shown clearly by Figure 36 and Figure 38.

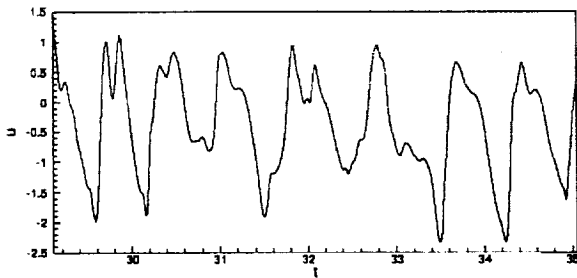


Figure 36: Instantaneous streamwise velocity at location point P3

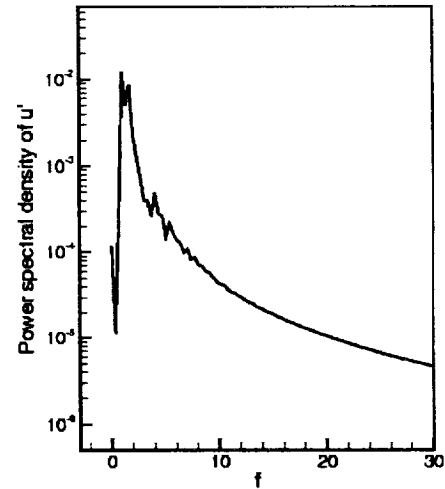


Figure 37: Power spectrum density of  $u'$  at location point P3

Point P9 locates right above the suction surface near the trailing edge. The instantaneous fluctuations of streamwise velocity and pressure at P9 and their power spectrum are displayed in Figure 40 – Figure 43. This area is controlled by the large scale trailing edge vortex, which is displayed clearly in Figure 30. No high-frequency oscillation is observed for both the streamwise velocity and pressure. It is also interesting to notice that the streamwise velocity is of opposite phase to pressure, i.e., the streamwise velocity decreases as pressure increases. At this point, the peak frequency of velocity is  $f = 0.11$ , which is almost the same for pressure. This number is thought to be the frequency for the large-scale trailing edge vortex.

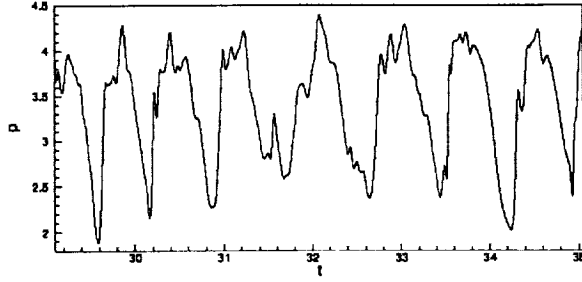


Figure 38: Instantaneous pressure at location point P3

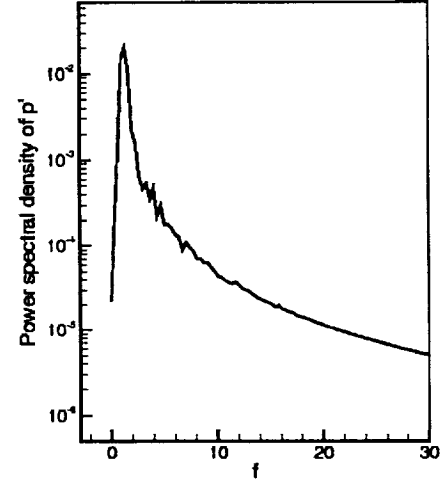


Figure 39: Power spectrum density of  $p'$  at location point P3

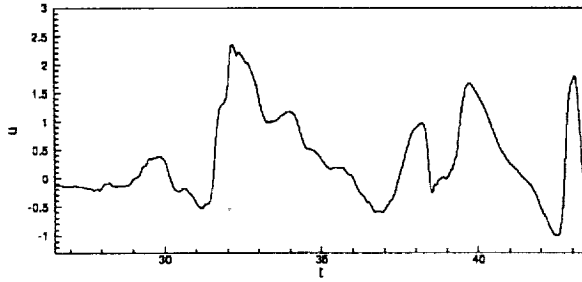


Figure 40: Instantaneous streamwise velocity at location point P9

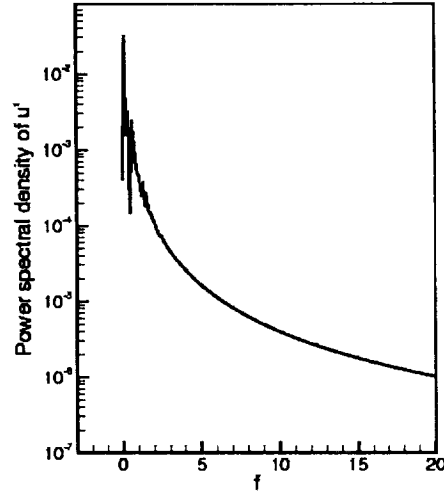


Figure 41: Power spectrum density of  $u'$  at location point P9

Now we focus on the next location point P11, which locates in the wake but still close to the trailing edge. High-frequency oscillations appear on streamwise velocity and pressure displayed in Figure 44 and 46, respectively. The oscillation parts are enlarged to obtain a clear view. The high-frequency oscillations are associated with the small-scale vortex structures appearing from the trailing edge along the downstream edge of the large-scale trailing edge vortex, as shown in frames (h), (i) (o), (p) of Figure 30. The high-frequency parts are modulated by the low-frequency signals corresponding to the large-scale trailing edge vortex. The high-frequency signals of streamwise velocity and pressure are displayed in Figure 48 to Figure 51. The high-frequency part is similar to signal of the Kelvin-Helmholtz type instability in the wake, which will be discussed in the next paragraph. The peak frequency for streamwise velocity is  $f = 12.67$ , which is same as pressure.

Generally speaking, the signals recorded at P12 are similar to P11, and the only difference is

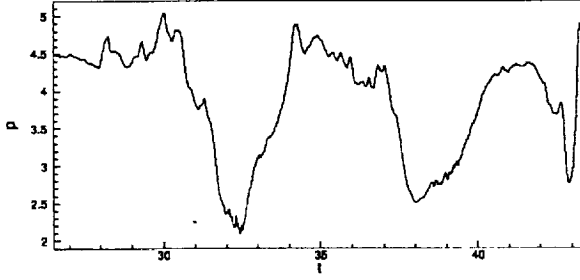


Figure 42: Instantaneous pressure at location point P9

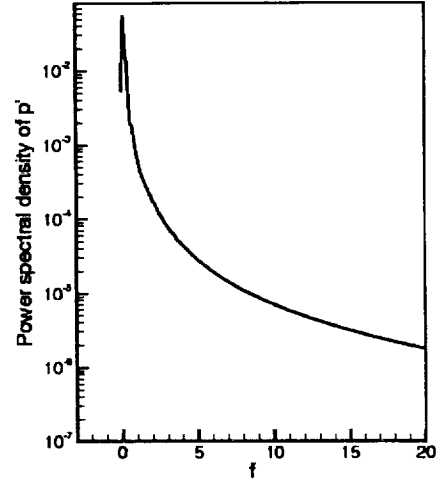


Figure 43: Power spectrum density of  $p'$  at location point P9

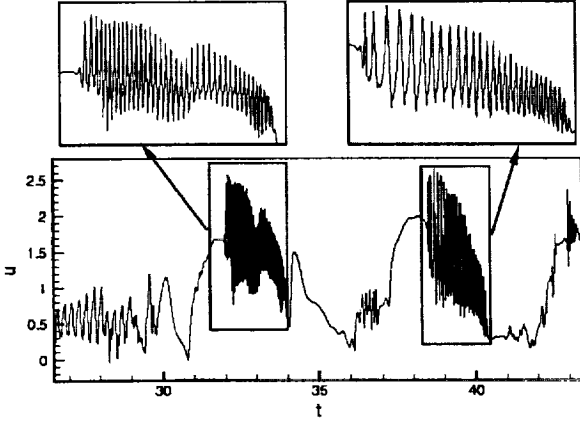


Figure 44: Instantaneous streamwise velocity at location point P11

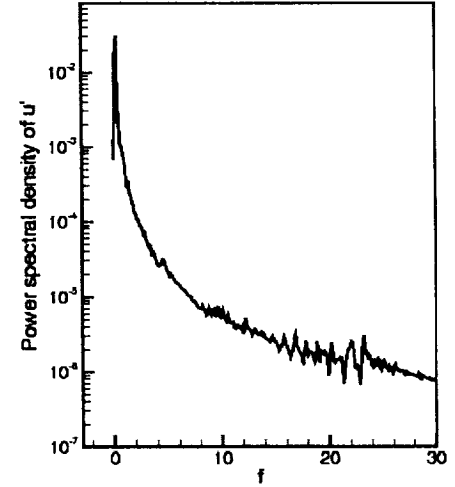


Figure 45: Power spectrum density of  $u'$  at location point P11

discovered at the initial stage, which is corresponding to frame (a) to (c) in Figure 30, where Kelvin-Helmholtz type instability is observed in the wake. The signals of streamwise velocity, pressure and their spectrums are displayed from Figure 52 to 55. The regular pattern of velocity and pressure is similar to the signal generated by vortex of typical Kelvin-Helmholtz type instability. The peak frequency is  $f = 5.2$  for velocity and  $f = 3.52$  for pressure.

## 5 Conclusions

Direct numerical simulation is carried out by solving the full Navier-Stokes equations in generalized curvilinear coordinates to study the separation flow around a NACA 0012 airfoil at large angle of

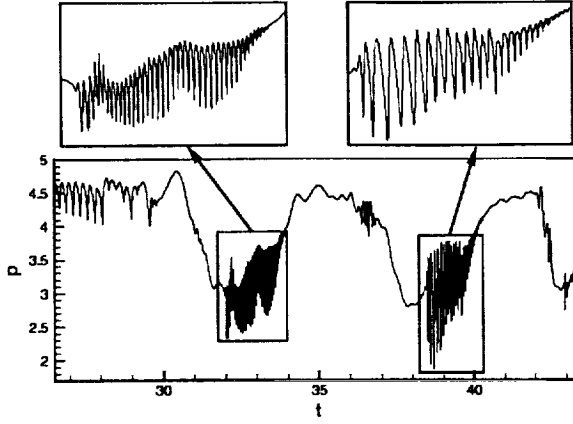


Figure 46: o  
nInstantaneous pressure at location point P11

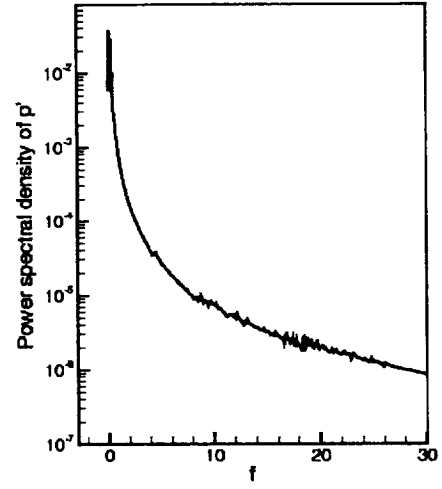


Figure 47: Power spectrum density of  $p'$  at location point P11

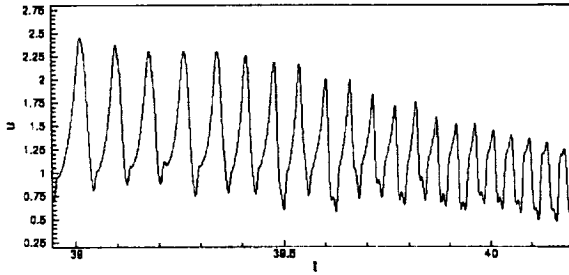


Figure 48: High-frequency part of the instantaneous streamwise velocity at location point P11

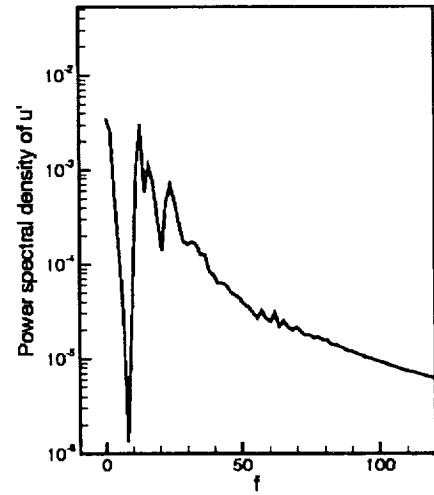


Figure 49: Power spectrum density of signal  $u'$  in Figure 48

attack. By using a fourth-order centered compact scheme for spatial discretization, the small-scale vortical structures are resolved, which will dissipate if low-order numerical schemes are used. Non-reflecting boundary conditions are imposed at the far-field and outlet boundaries to avoid possible non-physical wave reflection.

The DNS results clearly describe the flow separation process at the suction surface of the airfoil. The phenomena of the leading edge separation, vortex shedding, vortex reattachment, vortex pairing, generation of large-scale trailing edge vortex, and small-scale vortices associated with the Kelvin-Helmholtz type instability are observed through the DNS database. These phenomena are consistent with the experimental results obtained by Shih, *et al*, (1992, 1995). Based on the spectral analysis, the vortex shedding frequency, the frequency of the first vortex reattachment, and

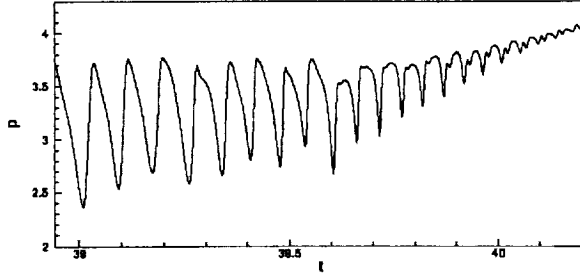


Figure 50: High-frequency part of the instantaneous pressure at location point P11

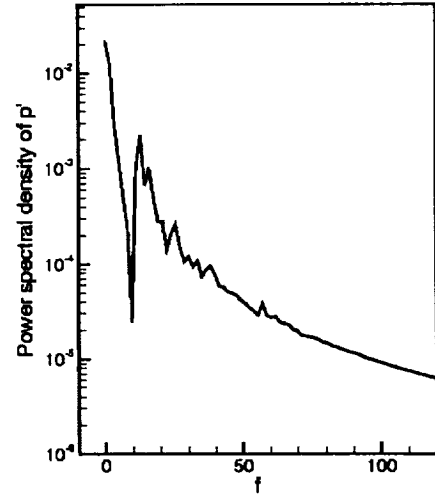


Figure 51: Power spectrum density of signal  $p'$  in Figure 50

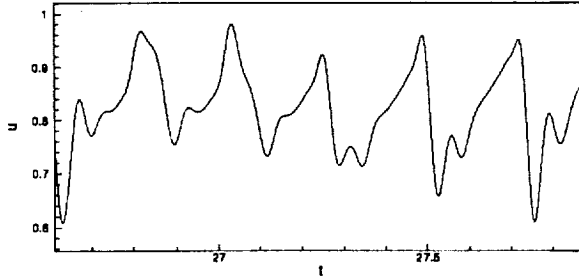


Figure 52: Early stage of the instantaneous stream-wise velocity at location point P12

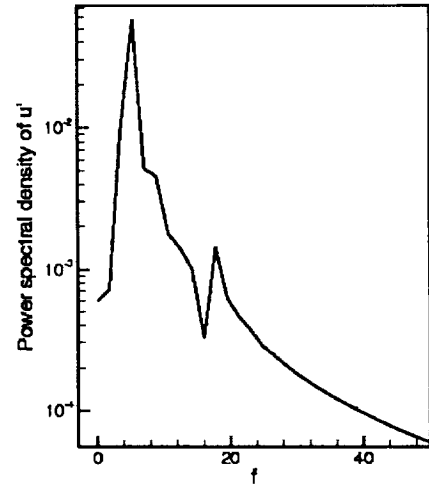


Figure 53: Power spectrum density of signal  $u'$  in Figure 52

the frequency of the generation of the large-scale trailing edge vortex are found. These information may be used to study the separation control, and the noise reduction.

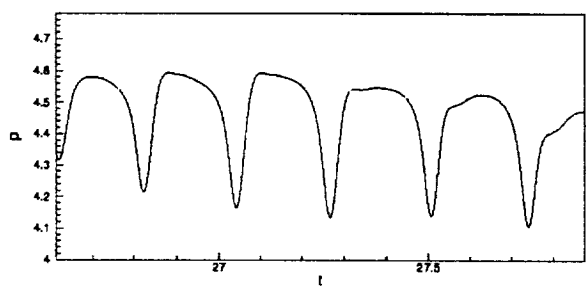


Figure 54: Early stage of the instantaneous pressure at location point P12

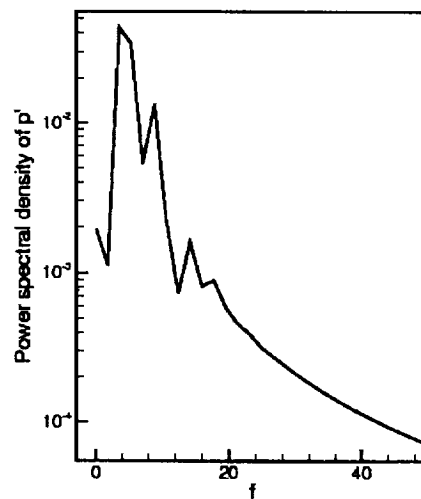


Figure 55: Power spectrum density of signal  $p'$  in Figure 54



## References

- [1] Arena, A. V., and Muellet, T. J. 1980. laminar separation, transition, and turbulent reattachment near the leading edge of airfoils. *AIAA Journal*, **18**(7), pp.747-753
- [2] Jiang, L., Shan, H, Liu, C., Visbal, M. R. 1999. Non-reflecting boundary condition in curvilinear coordinates, *Second AFOSR International Conference on DNS/LES*, Rutgers, New Jersey, June 7-9.
- [3] LeLe, S. K. 1992. Compact finite difference schemes with spectral-like resolution. *J. Comput. Phys.* **103**, pp.16-42.
- [4] Shih, C., Lourenco, L., Van Dommelen, L., and Krothapalli, A. (1992) Unsteady flow past an airfoil pitching at a constant rate. *AIAA Journal*, **30**(5), pp.1153-1161
- [5] Shih, C., Lourenco, and Krothapalli, A. (1995) Investigation of flow at leading and trailing edge of pitching-up airfoil. *AIAA Journal*, **30**(5), pp.1369-1376
- [6] Spekreijse, S.P. (1995) Elliptic grid generation based on Laplace equations and algebraic transformation. *J. Comp. Phys.*, **118**, pp.38-61
- [7] Tenaud, C., and Phuoc, L. T. 1997. Large eddy simulation of unsteady, compressible, separated flow around NACA 0012 airfoil. *Lecture Notes in Physics*. **490**, pp.424-429.
- [8] Thompson, J. F., Warsi, Z. U. A., and Mastin, C. W. 1985. *Numerical Grid Generation: Foundations and Applications*. Elsevier, New York
- [9] Wu, J-Z., Lu, X., Denny, A. G., Fan, M., and Wu, J-M. 1999. Post-stall flow control on an airfoil by local unsteady forcing. *J. Fluid Mech.*, **371**, pp.21-58.
- [10] Yoon, S., Kwak D. 1992. Implicit Navier-Stokes solver for three-dimensional compressible flows, *AIAA Journal* **30**, pp.2653-2659